

MSCN-NET: Multi-stage cascade neural network based on attention mechanism for Čerenkov luminescence tomography

Cite as: J. Appl. Phys. **132**, 173104 (2022); <https://doi.org/10.1063/5.0119787>

Submitted: 10 August 2022 • Accepted: 01 October 2022 • Published Online: 02 November 2022

Mengfei Du, Yi Chen, Weitong Li, et al.



View Online



Export Citation



CrossMark

ARTICLES YOU MAY BE INTERESTED IN

[A dual-axis high-order harmonic and single-axis phase-insensitive demodulation atomic magnetometer for in situ NMR detection of Xe](#)

Journal of Applied Physics **132**, 144401 (2022); <https://doi.org/10.1063/5.0096583>

Trailblazers. ^{New}

Meet the Lock-in Amplifiers that measure microwaves.

Zurich Instruments [Find out more](#)



MSCN-NET: Multi-stage cascade neural network based on attention mechanism for Čerenkov luminescence tomography

Cite as: J. Appl. Phys. **132**, 173104 (2022); doi: [10.1063/5.0119787](https://doi.org/10.1063/5.0119787)

Submitted: 10 August 2022 · Accepted: 1 October 2022 ·

Published Online: 2 November 2022



Mengfei Du,^{1,2} Yi Chen,^{1,2} Weitong Li,^{1,2} Linzhi Su,^{1,2,a)} Huangjian Yi,¹  Fengjun Zhao,¹ Kang Li,^{1,2} Lin Wang,³ and Xin Cao^{1,2,a)} 

AFFILIATIONS

¹School of Information Science and Technology, Northwest University, Xi'an, Shaanxi 710127, China

²National and Local Joint Engineering Research Center for Cultural Heritage Digitization, Xi'an, Shaanxi 710127, China

³School of Computer Science and Engineering, Xi'an University of Technology, Xi'an, Shaanxi 710127, China

^{a)}Authors to whom correspondence should be addressed: sulinzhi029@163.com and xin_cao@163.com

ABSTRACT

Čerenkov luminescence tomography (CLT) is a highly sensitive and promising technique for three-dimensional non-invasive detection of radiopharmaceuticals in living organisms. However, the severe photon scattering effect causes ill-posedness of the inverse problem, and the results of CLT reconstruction are still unsatisfactory. In this work, a multi-stage cascade neural network is proposed to improve the performance of CLT reconstruction, which is based on the attention mechanism and introduces a special constraint. The network cascades an inverse sub-network (ISN) and a forward sub-network (FSN), where the ISN extrapolates the distribution of internal Čerenkov sources from the surface photon intensity, and the FSN is used to derive the surface photon intensity from the reconstructed Čerenkov source, similar to the transmission process of photons in living organisms. In addition, the FSN further optimizes the reconstruction results of the ISN. To evaluate the performance of our proposed method, numerical simulation experiments and *in vivo* experiments were carried out. The results show that compared with the existing methods, this method can achieve superior performance in terms of location accuracy and shape recovery capability.

Published under an exclusive license by AIP Publishing. <https://doi.org/10.1063/5.0119787>

I. INTRODUCTION

The Čerenkov effect refers to the phenomenon in which charged particles in a medium emit visible light (named as Čerenkov radiation) when they travel faster than the speed of light in the medium.¹ Based on Čerenkov radiation, Čerenkov luminescence imaging (CLI) was proposed to image the distribution of radiopharmaceuticals in tissues.² Due to its advantages of low cost, non-invasive, and high throughput,^{3–5} CLI has attracted wide attention and has been successfully applied in clinical research, including early diagnosis of tumors, endoscopy, and clinical surgery.^{6–10} However, CLI is a two-dimensional imaging method similar to x-ray imaging; therefore, it could not achieve the depth information and the three-dimensional (3D) distribution of radioactive probes,¹¹ which limits the further application of CLI.

To give CLI the ability of 3D imaging, Čerenkov luminescence tomography (CLT) was proposed,¹² which can obtain three-dimensional distribution information of radioactive probes.^{13,14} However, the severe photon scattering effect causes ill-posedness of the inverse problem.¹⁵ To alleviate the ill-posed inverse problem in CLT reconstruction,¹⁶ researchers have carried out in-depth research, and some prior information^{17–20} was added to improve the reconstruction performance. For the animal structure prior, the first CLT reconstruction for small-animal imaging was conducted with a homogeneous mouse model by assuming that the optical properties were consistent and uniform,¹² but this assumption is not consistent with reality. Therefore, Hu *et al.* first employed the different properties of the biological tissues to establish a heterogeneous mouse model, which reduced the systematic error and showed a remarkable improvement of the tumor location

accuracy.²¹ For the Čerenkov spectrum prior, the multispectral reconstruction method divided the Čerenkov spectrum into several sub-spectral bands to reduce the ill-conditioned level of CLT reconstruction, which improved the reconstruction accuracy compared to the hybrid spectrum method.²² Based on the multispectral method and the optical characteristics of each sub-spectral band, a more accurate multispectral hybrid method was proposed by Liu *et al.*²³ In addition, some regularization methods were used for CLT reconstruction, such as L_2 -norm regularization,¹² L_1 -norm regularization,²⁴ and L_p -norm ($0 < p < 1$) regularization.²² However, these regularization methods still have some shortcomings. L_2 -norm regularization introduces many reconstructed artifacts, the result of reconstruction being over-smooth. L_1 -norm regularization and L_p -norm ($0 < p < 1$) regularization are over-sparseness and incomplete reconstruction of the radiation probe.²⁵ Recently, Mousavi *et al.* proposed an iterative convex refinement (ICR) approach to encourage the sparsity for signal recovery.²⁶ This work uses the sparsity of source reasonably and overcomes the problem of over-sparsity and over-smoothness in CLT reconstruction. A sparse-graph manifold learning (SGML) method was proposed for CLT.²⁷ Although these strategies improve the performance of CLT reconstruction, the deviation between the simplified light propagation model and the actual photon propagation process still limits the accuracy of CLT reconstruction.

Recently, methods based on deep learning have been widely used in optical tomographic reconstruction. Different from model-based methods, neural networks can directly learn the mapping relation between the surface photon intensity and the Čerenkov source distribution. A gated recurrent unit based network was proposed to improve the accuracy and speed of single-source reconstruction.²⁸ A 3D encoder-decoder network is used for fluorescence molecular tomography (FMT) reconstruction.²⁹ Meanwhile, Zhang *et al.* applied a multi-layer fully connected neural network (MFCNN) to reconstruct the distribution of Čerenkov sources.³⁰ Cao *et al.* proposed a stacked denoising autoencoder (SDAE) framework to constantly update the permissible domain for CLT reconstruction.³¹ Meng *et al.* proposed a local connection network based on K-Nearest Neighbor (KNN) for FMT reconstruction (KNN-LC), which improved the accuracy and stability of FMT reconstruction.³² Zhang *et al.* applied an attentional local connection network to CLT reconstruction (AMLC), which further improved the accuracy of reconstruction.³³ In addition, Zhang *et al.* proposed a residual neural network for accurate and stable reconstruction in CLT.³⁴ All existing optical reconstruction methods based on deep learning directly establish the mapping relationship between the surface photon intensity and the Čerenkov source distribution. However, CLT is divided into two processes: forward propagation and backward reconstruction. The forward propagation process of light can be described by the radiative transfer equation (RTE), which satisfies the physical regulation. In the physical neural network (PINNS),³⁵ the physical regulation plays a strong role of constraint. Inspired by the physical neural network, we believe that introducing the forward process can play a vital role of constraint on the reconstruction network so that CLT reconstruction can meet the physical regulation.

In this study, a multi-stage cascade network (MSCN-NET) is proposed for CLT reconstruction. MSCN-NET cascades an inverse

sub-network (ISN) and a forward sub-network (FSN), the ISN is used to learn the mapping between the surface photon intensity and the Čerenkov source distribution, and the FSN is used to derive the surface photon intensity from the Čerenkov source distribution. The network structure of ISN is divided into several sub-modules, each of which contains the attention layer and the forward feedback layer based on residuals. Particularly, the surface photon intensity is regarded as a node feature, and the attention mechanism enables us to notice some more important features, where nodes with larger energy values will be given more weight. In addition, FSN is a multi-layer fully connected neural network, which is used to deduce the surface photon intensity from the reconstructed source distribution. To improve the performance of CLT reconstruction, the ISN is jointly constrained by the loss of FSN and ISN.

The main structure of the rest of this paper is as follows: Sec. II introduces the network structure and evaluation indicators, Sec. III designs digital simulation experiments and *in vivo* implanted experiments to prove the effectiveness of our method, and Sec. IV summarizes and discusses this work.

II. METHODOLOGY

A. Model-based CLT reconstruction

In the model-based reconstruction method, the radiative transfer equation (RTE) is used to describe the transmission process of light in the organism.²⁵ Because RTE contains multiple variables, it is difficult to solve complex biological tissues. Therefore, researchers proposed a simplified diffusion approximation (DA) equation to describe the optical transmission process,^{36,37} which has been widely used in CLT, as well as other optical molecular tomography. The DA model combined with the Robin boundary condition can be expressed as^{38,39}

$$\begin{cases} -\nabla \cdot (D(r) \cdot \nabla \Phi(r)) + \mu_a(r)\Phi(r) = S(r), & (r \in \Omega), \\ \Phi(r) + 2A(r, n, n')D(r)(\nu(r) \cdot D(r)) = 0, & (r \in \partial\Omega), \end{cases} \quad (1)$$

where r is the position vector, $D(r)$ is the diffusion coefficient of position vector r , $\Phi(r)$ is the photon flux density of position vector r , μ_a is the absorption coefficient, $S(r)$ is the internal source distribution of position vector r , Ω represents the solution domain, $\partial\Omega$ represents the boundary of the domain, A is the boundary mismatch factor between the biological tissues and the surrounding medium, and $\nu(r)$ denotes the unit outer normal on $\partial\Omega$. $D(r)$ and $A(r, n, n')$ are calculated as follows:

$$D(r) = \frac{1}{3(\mu_a(r) + (1-g)\mu_s(r))}, \quad (2)$$

$$A(r, n, n') \approx \frac{1+R(r)}{1-R(r)}, \quad (3)$$

where $\mu_a(r)$ denotes the optical absorption coefficient, $\mu_s(r)$ denotes the optical scattering coefficient, g is the medium anisotropy factor, $R(r)$ is the inner reflection coefficient, n is the refractive index within Ω , and n' is the refractive index of an external

medium. The diffusion equation is discretized by the finite element method,^{40,41} and the following linear relation can be obtained:

$$UX = \varphi, \tag{4}$$

where U represents the system matrix. X represents the distribution of Čerenkov sources within the organism, and φ is the intensity of photons on the surface of the organism.

B. Deep learning-based CLT reconstruction

In the method based on deep learning, the neural network is used to establish the mapping relationship between the photon intensity on the surface of the organism φ and the distribution of the Čerenkov source inside the organism X , which is defined as follows:

$$\min \|f_m(\varphi|\theta) - X\|_2^2, \tag{5}$$

where f_m denotes the neural network used for CLT reconstruction and θ denotes the network weight. We can update the network weight θ by minimizing the mean square error between the reconstructed and real sources.

C. Multi-stage cascade neural network based on an attention mechanism

Our MSCN-NET is mainly cascaded by the ISN and FSN. The ISN is used to establish mapping between the surface photon

intensity and the distribution of the Čerenkov source, and the FSN is used to derive the surface photon intensity from the reconstructed source distribution, which conforms to the regulation of photon transmission. Specifically, the surface photon intensity is first fed to the ISN to obtain the reconstructed source, and then the reconstructed source is fed to the FSN to obtain the surface photon intensity. The structure of MSCN-NET is shown in Fig. 1. The ISN is composed of two sub-modules, each includes an attention layer and a forward feedback layer, which also includes layer normalization and residual connection. The FSN consists of four fully connected layers, which are used to deduce the surface photon intensity from the radiation source distribution. The main purpose of FSN is to improve the performance of ISN. Particularly, the input and output dimensions of the ISN and FSN are the number of nodes in the mesh model. In addition, when training MSCN-NET, train the ISN first and then add FSN to the training when the ISN is stable. Since the input of FSN is the reconstructed Čerenkov source of the output of ISN and FSN plays a constraint role on ISN, inspired by generative adversarial networks (GANs), when training MSCN-NET, we train it in stages. First, the ISN sub-network is trained to be stable to obtain a relatively accurate reconstruction source, and then the FSN subnetwork is added to the training to further optimize the reconstruction source.

The subnetwork ISN takes the photon intensity of each node as the feature of the node. In order to make the neural network pay attention to some more important node features, we introduce the attention mechanism. The specific operation of the attention mechanism is as follows. There are three different vectors, namely, query

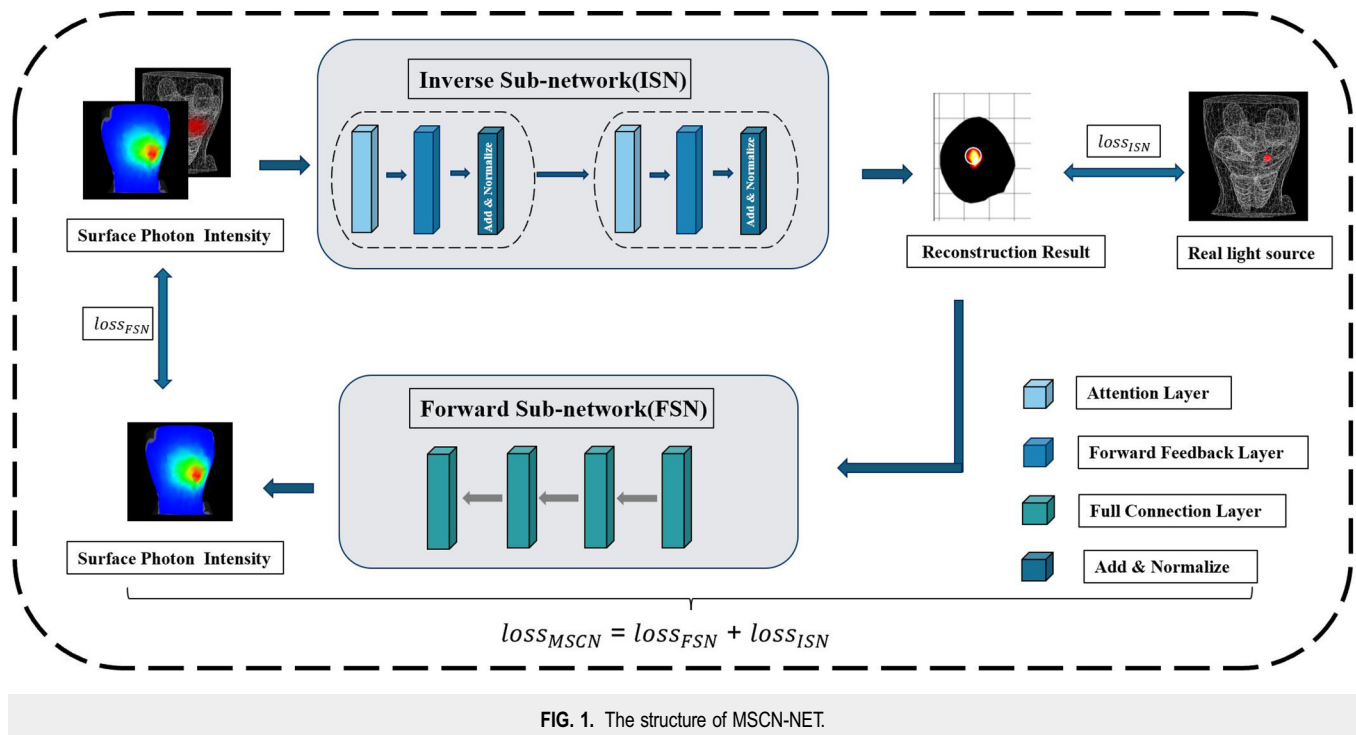


FIG. 1. The structure of MSCN-NET.

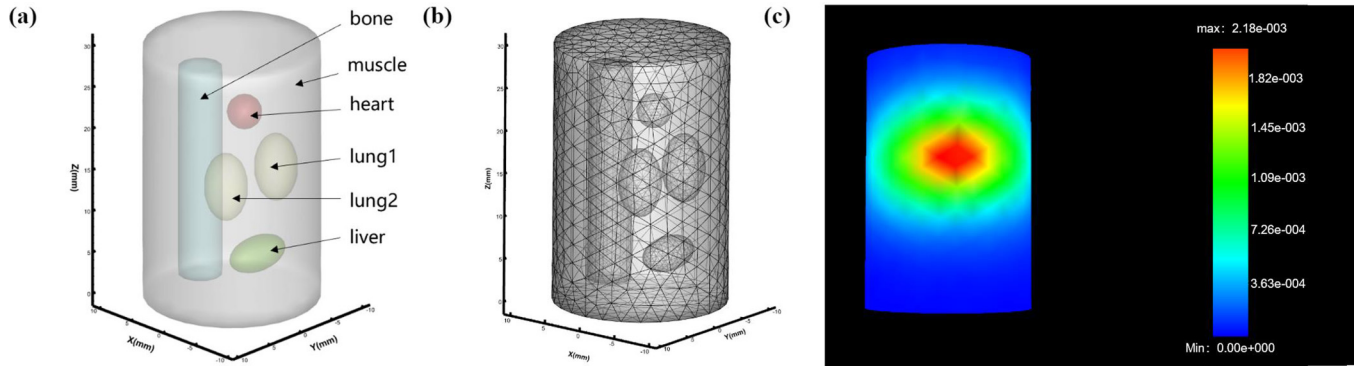


FIG. 2. The numerical phantom. (a) shows the numerical phantom-based physical model, (b) shows the standard mesh, and (c) shows the forward simulation result.

vector Q , key vector K , and value vector V , which are obtained by embedding vector T multiplied by three different weight matrices W^q , W^k , and W^v . After obtaining Q , K , and V , a feature vector Z is finally obtained through calculation, and its definition is as follows:

$$Z = \text{softmax}\left(\frac{QK^T}{\sqrt{d_K}}\right)V. \quad (6)$$

The subnetwork FSN takes the reconstructed source distribution of the ISN output as the input and the surface photon intensity as the output. That is, the network is used to learn the mapping relation of the photon intensity from the radiation source to the surface, and this relation conforms to the regulation of light transmission. In particular, we add the error between the surface photon intensity obtained by FSN and the original surface photon intensity into loss function as a loss term, which is defined as follows:

$$\min \|f_{ISN}(\varphi|\theta_1) - X\|_2^2 + \|f_{FSN}(X_{ISN}|\theta_2) - \varphi\|_2^2, \quad (7)$$

where f_{ISN} represents the inverse sub-network, θ_1 represents the weight of the ISN, φ represents the surface photon intensity, and X represents the distribution of radiation sources. f_{FSN} represents the forward sub-network, where θ_2 represents the weight of the FSN and X_{ISN} represents the reconstructed radiation source distribution.

D. Implementation details and evaluation metrics

The training and test of MSCN-NET were implemented using PaddlePaddle⁴² and Python 3.7. All operations were performed on a personal computer with an AMD Ryzen 7 1700 eight-core processor 3.00 GHz CPU and an NVIDIA GeForce GTX 3060 Ti GPU. The optimization function of MSCN-NET was a Stochastic Gradient Descent (SGD) optimizer with a learning rate of 0.0005.

In order to quantitatively evaluate the performance of the MSCN-NET network, we adopt the location error (LE), the Dice coefficient, and the relative intensity error (RIE) as evaluation indexes. LE represents the positional error between the reconstructed radioactive source and the actual radioactive source, which

is defined as follows:

$$LE = \|L_r - L_a\|, \quad (8)$$

where L_r denotes the barycenter coordinate of the reconstructed radioactive source and L_a denotes the barycenter coordinate of the actual radioactive source. The Dice coefficient is used to evaluate the accuracy of Čerenkov source morphology recovery in CLT reconstruction, and its definition is as follows:

$$\text{Dice} = \frac{2|X \cap Y|}{|X| + |Y|}, \quad (9)$$

where X denotes the reconstructed radiation source region and Y denotes the actual radiation source region. Dice coefficient values range from 0 to 1, with closer to 1 indicating better shape recovery. RIE is used to evaluate the relative intensity error between the reconstructed radioactive source intensity and the actual Čerenkov source intensity,

$$\text{RIE} = \frac{|I_r \cap I_a|}{I_a}, \quad (10)$$

where I_r denotes the intensity of the reconstructed source and I_a denotes the intensity of the actual source. Obviously, the closer the RIE is to 0, the better the intensity recovery of the reconstructed source. The contrast to noise ratio (CNR) is used to evaluate the

TABLE I. Optical coefficients used in numerical simulations.

Tissues	μ_a (mm ⁻¹)	μ_s (mm ⁻¹)	g
Muscle	0.016	0.510	0.90
Heart	0.011	1.053	0.86
Bone	0.021	2.864	0.90
Liver	0.065	0.723	0.90
Lung	0.036	2.246	0.90

TABLE II. Quantitative comparison of a single-source simulation (mean ± SD).

Method	LE	Dice	RIE	CNR
MSCN-NET	0.41 ± 0.22	0.65 ± 0.14	0.19 ± 0.12	0.72 ± 0.11
MFCNN	0.53 ± 0.25	0.51 ± 0.17	0.49 ± 0.17	0.42 ± 0.19
IVTCG	0.76 ± 0.28	0.41 ± 0.21	0.72 ± 0.24	0.23 ± 0.21

quality of reconstruction results, and CNR is defined as follows:

$$CNR = \frac{|\mu_R - \mu_B|}{(m_R\sigma_R^2 + m_B\sigma_B^2)^{1/2}}, \quad (11)$$

where μ_R and μ_B represent the mean values in the Region Of Interest (ROI) and background, respectively; σ_R^2 and σ_B^2 represent the variances; and m_R and m_B represent the number of nodes included in the ROI and background, respectively. The higher value of CNR indicates better quality of the reconstruction.

III. EXPERIMENTS AND RESULTS

To verify the performance of MSCN-NET in CLT reconstruction, two groups of numerical simulation experiments and one group of *in vivo* experiments were conducted in this section. The numerical simulation experiments include a single-source experiment and a double source experiment. At the same time, the practicability of MSCN-NET was verified by *in vivo* experiments. In addition, Incomplete Variables Truncated Conjugate Gradient

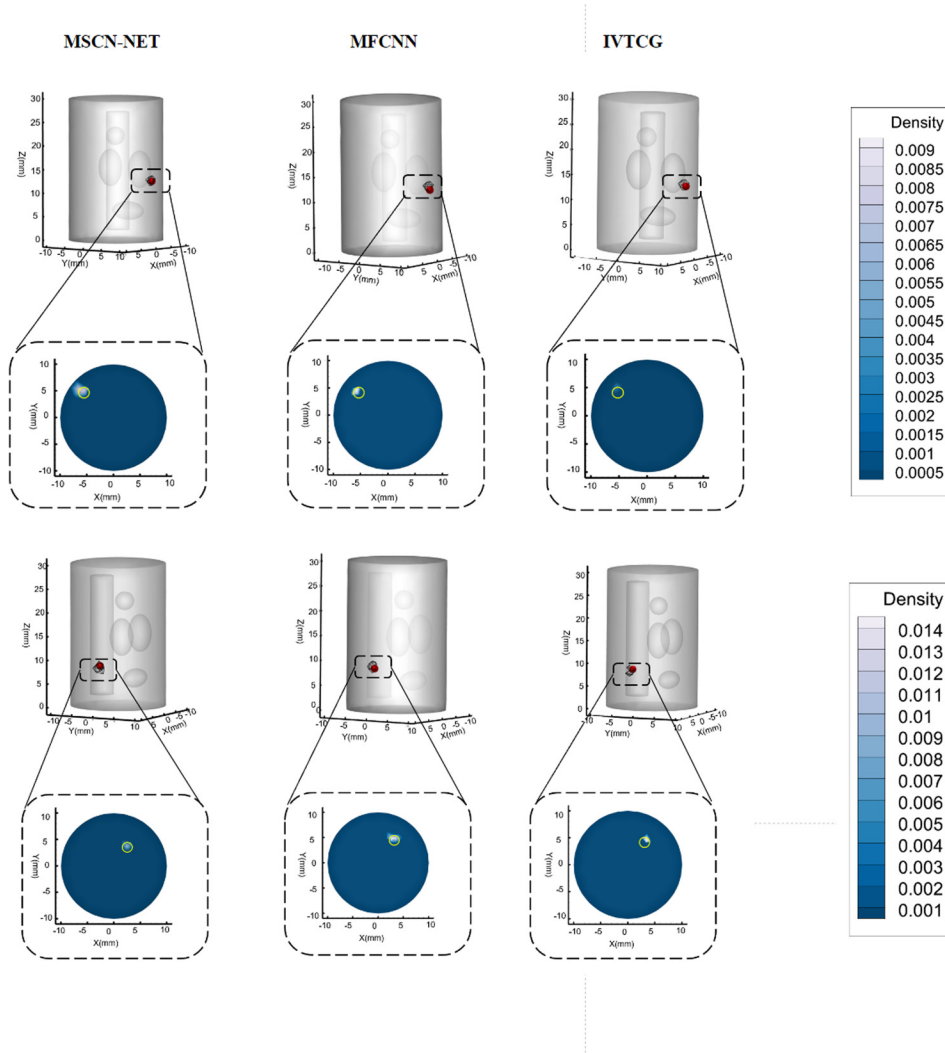


FIG. 3. The quantitative results of single-source samples. Represent quantization values of LE, Dice, RIE, and CNR, respectively.

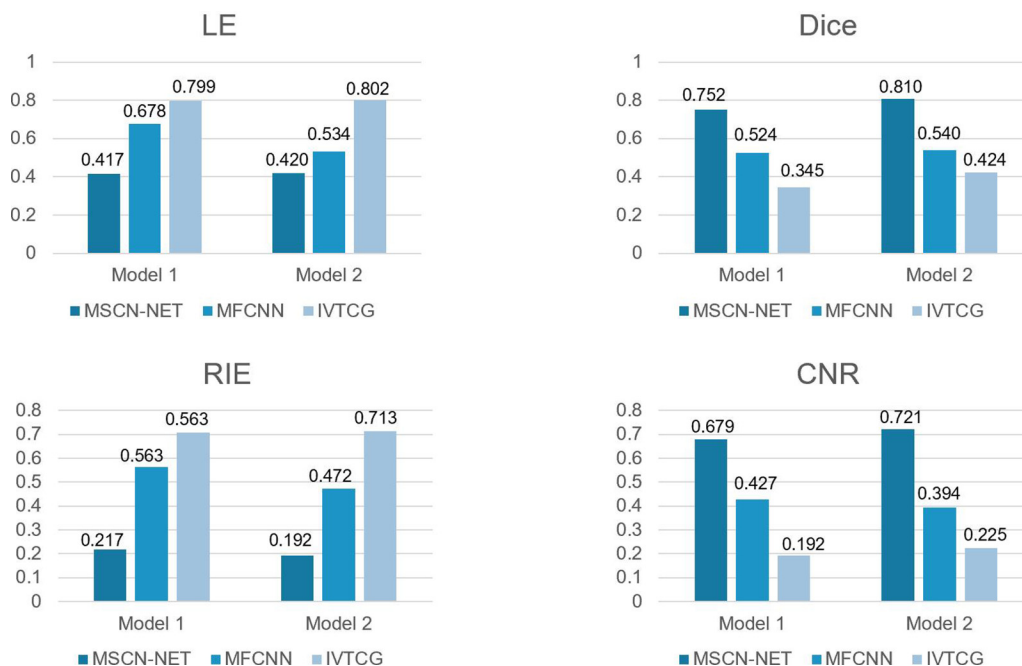


FIG. 4. Comparison results of single-source numerical simulation experiments. The red color in the cylindrical model represents the location of the original Čerenkov source. The cylindrical model was cut along the z axis of the Čerenkov source to obtain an axial view, where yellow circles represent the actual position and size of the Čerenkov source.

(IVTCG) and MFCNN were used as the baseline for comparison in the above experiments.^{30,43}

A. Numerical simulation experiments

1. Data collection

In the numerical simulation experiment, we adopted a cylindrical model with a height of 30 mm and a radius of 10 mm to simulate the body of a living creature. The cylinder model mainly includes five organs: heart, bone, liver, lung, and muscle, as shown in Fig. 2(a). The optical parameters of all organs are shown in Table I, which are taken from the literature.⁴⁴ Meanwhile, COMSOL Multiphysics software was used to discretize the model into a unified tetrahedral mesh,⁴⁵ which contained 4626 nodes and 25 840 tetrahedral units, as shown in Fig. 2(b). A small ball with a diameter of 1 mm was set to represent the Čerenkov source, where the photon wavelength was set to 650 nm. As a data-driven method, the neural network requires a large amount of data for training. The surface light flux distribution of all samples was simulated through the Molecular Optical Simulation Environment (MOSE 2.3) platform,⁴⁶ as shown in Fig. 2(c). Considering that Čerenkov sources may be in any part of the model, simulation samples should cover the whole model as much as possible. Therefore, 203 single-source samples were simulated. In addition, by randomly combining two samples from single-source data to create a dual-source sample, the surface photon intensity of the dual source and the distribution of the Čerenkov source are

calculated as follows:

$$\varphi_{dual} = \sum_{i \in S_n} \varphi_i, \tag{12}$$

$$X_{dual} = \sum_{i \in S_n} X_i, \tag{13}$$

where φ_{dual} represents the surface photon intensity of the double source, X_{dual} represents the distribution of the dual-source sample, φ_i represents the surface photon intensity of the i th single Čerenkov source, X_i represents the distribution of the i th single-source sample, and S_n represents the collection of samples of the single source.

In summary, in this work, 203 single-source samples were simulated and 5000 dual-source samples were created. 80% of the data were used for training and the rest for testing.

TABLE III. Quantitative comparison of a dual-source simulation (mean \pm SD).

Method	LE	Dice	RIE	CNR
MSCN-NET	0.58 \pm 0.18	0.54 \pm 0.1	0.24 \pm 0.15	0.37 \pm 0.12
MFCNN	0.71 \pm 0.21	0.37 \pm 0.21	0.47 \pm 0.19	0.24 \pm 0.14
IVTCG	0.89 \pm 0.28	0.25 \pm 0.26	0.69 \pm 0.24	0.17 \pm 0.19

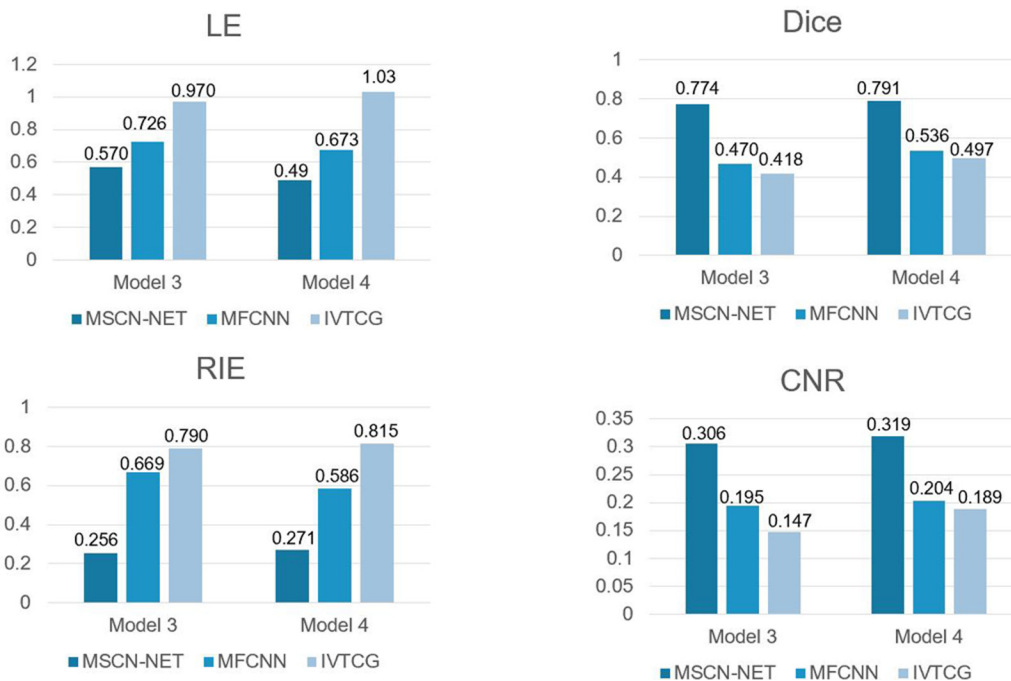


FIG. 5. The quantitative results of dual-source samples. Represent the quantitative value of LE, Dice, RIE, and CNR, respectively.

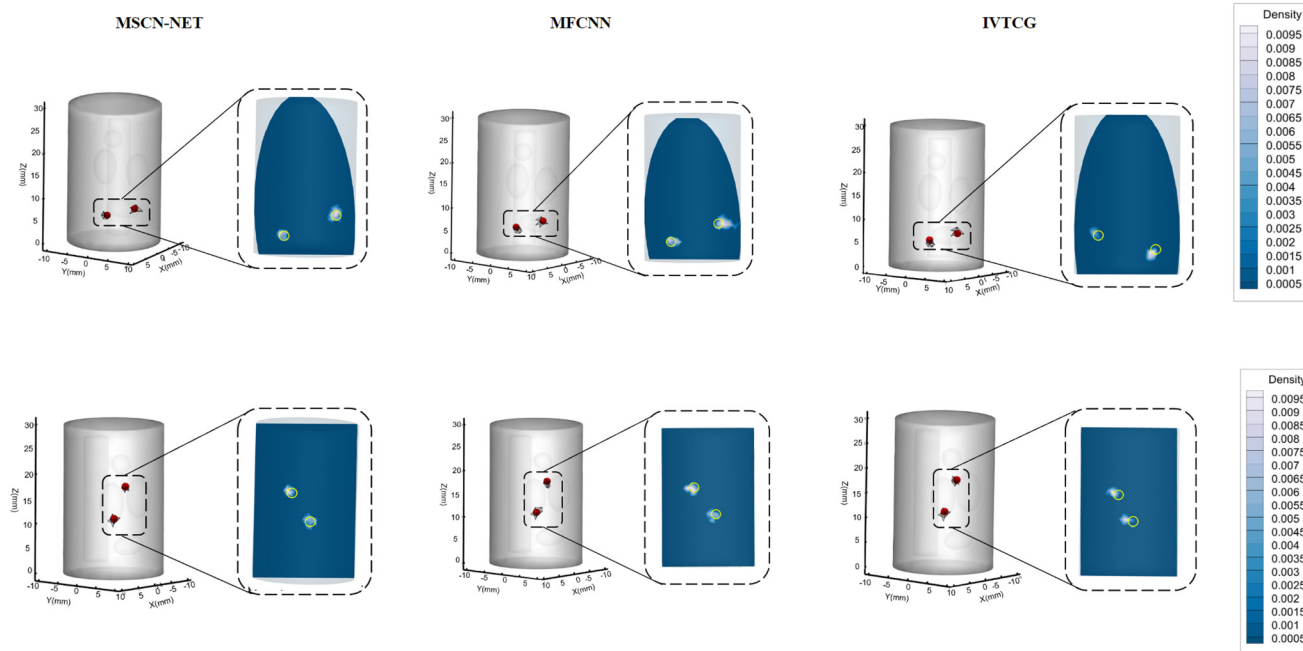


FIG. 6. Comparison results of the dual-source numerical simulation experiments. The red color in the cylindrical model represents the location of the original Čerenkov source. The cylindrical model was cut along the x axis of the Čerenkov source, where yellow circles represent the actual position and size of the Čerenkov source.

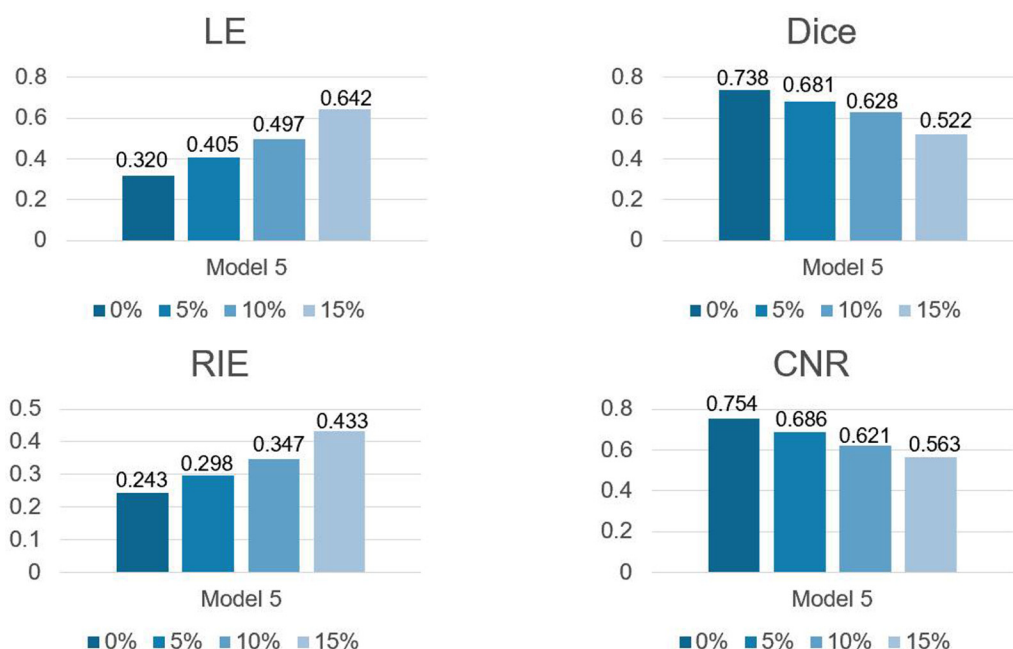


FIG. 7. Anti-noise experiment of CLT reconstruction. The experimental results of adding 5%, 10%, and 15% noise are shown.

2. Single-source simulation experiments

To verify the shape recovery ability of our method, we compare the reconstruction performance of MSCN-NET, MFCNN, and IVTCG in a spherical single Čerenkov source. At the same time, we calculated the average value and the deviation of different evaluation indexes as shown in Table II. Experimental results show that MSCN-NET achieves the highest average positioning accuracy, the highest DICE coefficient, and the smallest RIE. Experimental results show that the MSCN-NET has good positioning accuracy, morphological recovery ability, and an energy intensity recovery rate.

Two samples, Model 1 and Model 2, whose Čerenkov source coordinates are $(-6, 5, 12)$ and $(3, 4, 8)$ mm, were used to measure the single-source reconstruction results of different methods. The quantitative results of CLT reconstruction are shown in Fig. 3. Figure 4 shows the reconstruction results obtained by MSCN-NET, MFCNN, and IVTCG, respectively, which shows that the MSCN-NET has good performance in positioning accuracy, morphological recovery ability, and an energy intensity recovery rate.

3. Dual-source simulation experiments

In order to measure the positioning accuracy of MSCN-NET, we compare the reconstruction performance of MSCN-NET, MFCNN, and IVTCG in a dual source. At the same time, we calculated the average value and the deviation of different evaluation indexes as shown in Table III. Experimental results show that MSCN-NET still has advantages in LE, Dice, and RIE.

Two samples, Model 3 and Model 4, were used to measure the dual-source reconstruction results of different methods. In

Model 3, the centers of a dual source were set at $(3, 3, 16)$ and $(-2, -5, 6)$ mm, respectively. In Model 4, the sources were set at $(1, 3, 7)$ and $(-1, 2, 18)$ mm. The quantitative results are shown in Fig. 5. Figure 6 shows the reconstruction results obtained by MSCN-NET, MFCNN, and IVTCG, respectively, which is consistent with the results of a single-source experiment. The experimental results show that the reconstructed source shape of MSCN-NET is clear and easy to identify.

4. Anti-noise experiment

To verify the stability of MSCN-NET, we have carried out anti-noise experiments, taking Model 5 as an example, whose

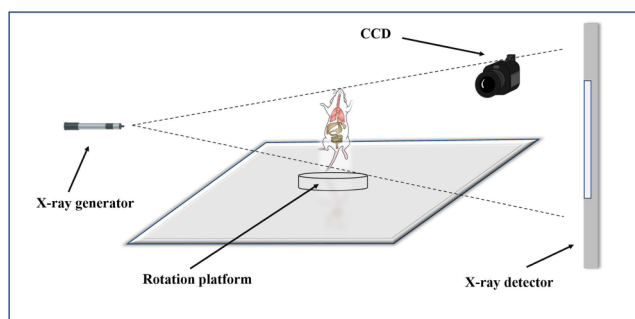


FIG. 8. The schematic diagram of a device structure of a CLT/micro-CT dual-mode system.

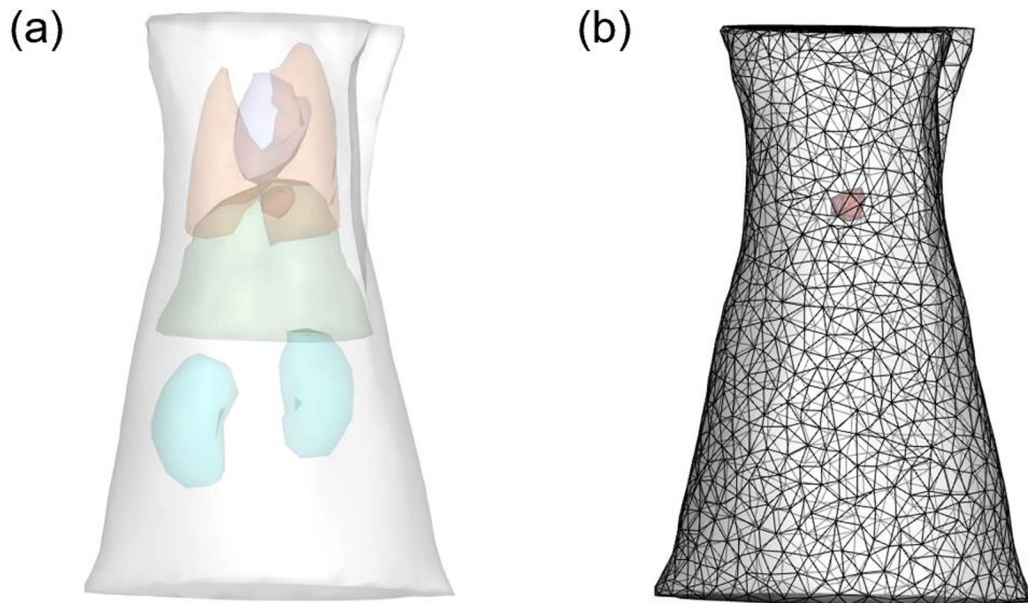


FIG. 9. The *in vivo* mouse model is shown in Fig. 9(a), and Fig. 9(b) shows the distribution of the Čerenkov source at a certain location in the mouse body.

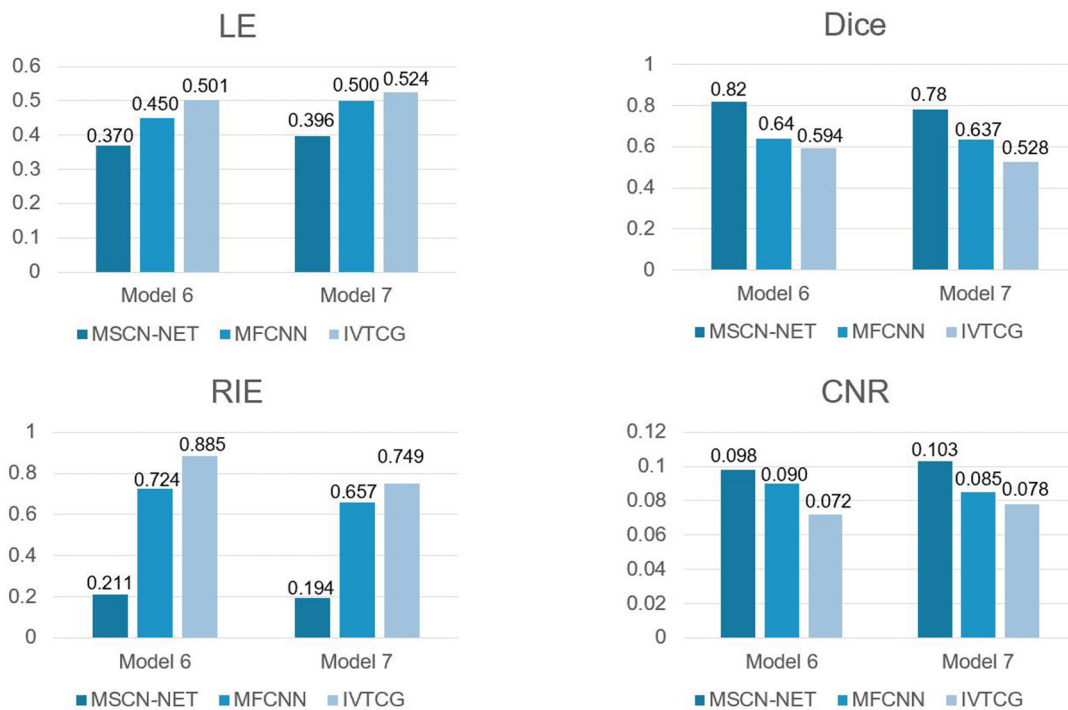


FIG. 10. The quantitative results of the *in vivo* experiments. Represent the quantitative value of LE, Dice, RIE, and CNR, respectively.

Čerenkov light source coordinates are (2, 2, 8) mm. Three different levels of Gaussian noise were added: 5%, 10%, and 15%, respectively. The experimental results are shown in Fig. 7. Although LE and RIE increased and Dice and CNR decreased after adding noise, position and morphology information could be recovered. The results prove the robustness of MSCN-NET.

B. *In vivo* reconstruction

In order to further evaluate the practicability of this method, we conducted *in vivo* implanted experiments. The experimental data were from the CLT/micro-CT dual-modal system on an adult

nude mouse, and the mouse was scanned with micro-CT. An implanted 7.4 MBq of an ^{18}F -FDG radioactive source was used to mimic the lesion containing a radionuclide probe. The mouse was placed on the automatic rotating stage, which was rotating 360° with 1° intervals to capture the images of CLI and x-ray projection. Using band-pass filters (FF01-650/13-25, Semrock, USA). The CLI signal with a wavelength of 650 nm and white light data were collected by cooled high-sensitivity EMCCD (−80 °C, iXonEM Ultra 888, UK). Before the acquisition process of CLI, long exposure time (5 min), a high given value (300), a high shift speed (13 μs), and a low speed readout rate (1 MHz at 16 bits) are set. Then, CT

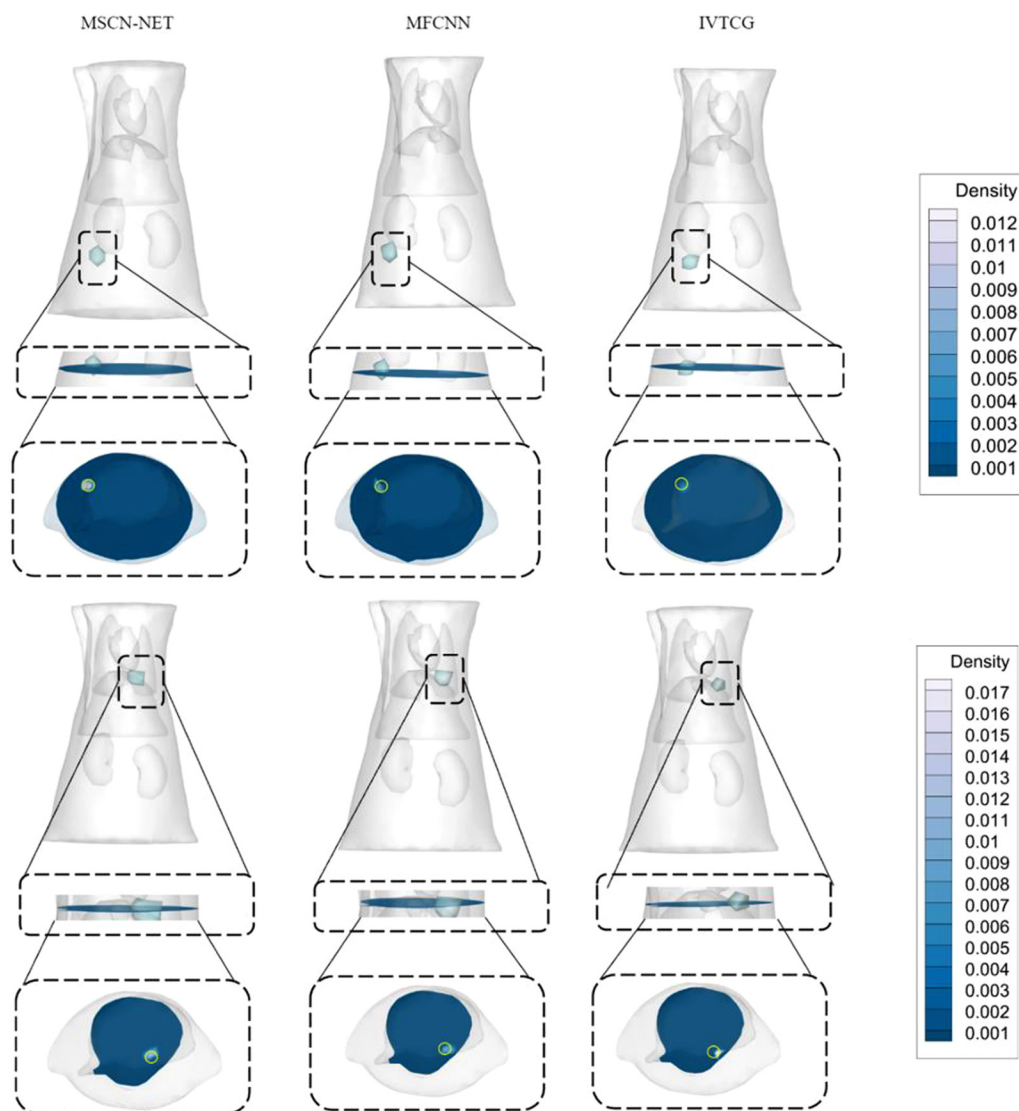


FIG. 11. Reconstruction results of different methods of *in vivo* experiments. The box under the 3D viewing angle represents the cutting surface, and after the cutting plane was enlarged, the axial viewing plane on the lower was obtained, and the yellow circle in the plane view was the real position and size of the Čerenkov source.

volume data were acquired by a micro-CT system (a tube voltage of 40 kVp and a tube current of 300 mA). The schematic diagram of the device structure of a CLT/micro-CT dual-mode system is shown in Fig. 8.

After reconstruction and segmentation, we obtained the trunk sections of the mouse with a height of 41 mm as shown in Fig. 9(a). Figure 9(b) shows the distribution of the Čerenkov source at a certain location in the mouse body. We segmented the main organs of the mouse, including muscle, lung, heart, stomach, liver, and kidney, and integrated these organs into the mouse model. Animal care and protocols were approved by the Fourth Military Medical University Animal Studies Committee. All surgical and imaging procedures were performed under isoflurane gas anesthesia, and all efforts were made to reduce the pain of experimental mice. The optical parameters of each organ are consistent with those in the literature.⁴⁷

Two samples, Model 6 and Model 7, whose Čerenkov source coordinates are (14.5, 14, 9) and (20.5, 24.5, 28.5) mm, were used to measure the *in vivo* results of different methods. The quantitative results are shown in Fig. 10. Figure 11 shows the reconstruction results obtained by MSCN-NET, MFCNN, and IVTCG, respectively, which is consistent with the results of the numerical simulation experiments. *In vivo* experiments show that the reconstructed source shape of MSCN-NET is clear and easy to identify, and the MSCN-NET has good practicability.

IV. DISCUSSION AND CONCLUSION

CLT is a promising imaging method to obtain the three-dimensional distribution of radiation probes. However, the traditional model-based CLT reconstruction method has some problems, such as a complex solution process and a large approximation error, which seriously affect its application. On the contrast, the existing reconstruction methods based on neural networks directly establish the mapping relationship between the surface photon intensity and the Čerenkov source without taking into account the influence of the CLT forward process. In this paper, we propose MSCN-NET for CLT reconstruction, which introduces a CLT forward process to feed the reconstructed source of ISN into the FSN to obtain the surface photon intensity. FSN is used to derive the surface photon intensity from the reconstructed source distribution, which is similar to the CLT forward process.

In order to verify the performance of MSCN-NET, we conducted digital simulation experiments, including a single-source experiment and a dual-source experiment. The traditional model-based method IVTCG and the neural network-based method MFCNN are used as a comparison. Experimental results show that MSCN-NET has the best localization ability and morphology recovery ability. Meanwhile, to further verify the practicability of MSCN-NET, glial mice were used for *in vivo* experiments. The results show that MSCN-NET performs well both in numerical simulation experiments and *in vivo* experiments.

To the best of our knowledge, MSCN-NET is the first network to introduce a forward process into the reconstruction process, which further constrains the reconstruction results. All the existing neural network-based methods directly learn the mapping relationship between the surface photon distribution and the internal

source distribution, while MSCN-NET introduces the forward process as a special constraint to improve the localization ability and the shape recovery ability of CLT reconstruction. However, there are still some defects that limit its application. MSCN-net is still a data-driven network, and the reconstruction performance is affected by the quantity and quality of data sets. In particular, there is still an error between the standard mesh and the actual structure, and additional optimization methods are needed to balance the error between the standard mesh and the actual structure. Combining neural networks and model-based approaches may overcome these limitations, which will be explored in future work.

In summary, we propose a MSCN-NET for CLT reconstruction and introduce a forward process to optimize the reconstruction results. The results show that MSCN-NET has good performance both in numerical simulations and *in vivo* experiments. This method is the first to introduce the forward process into the reconstruction process, and we believe that this new method will be helpful to improve the performance of CLT reconstruction and promote the application of CLT in biological research.

ACKNOWLEDGMENTS

National Key Research and Development Program of China (2019YFC1521102); National Natural Science Foundation of China (61701403, 61806164, 62101439, 61906154); China Postdoctoral Science Foundation (2018M643719); Natural Science Foundation of Shaanxi Province (2020JQ-601); Young Talent Support Program of the Shaanxi Association for Science and Technology (20190107); Key Research and Development Program of Shaanxi Province (2019GY-215, 2021ZDLSF06-04); Major research and development project of Qinghai (2020-SF-143).

AUTHOR DECLARATIONS

Conflict of Interest

The authors have no conflicts to disclose.

Author Contributions

Mengfei Du: Formal analysis (equal); Investigation (equal); Methodology (equal); Writing – original draft (equal). **Yi Chen:** Methodology (equal); Writing – review & editing (equal). **Weitong Li:** Investigation (equal). **Linzhì Su:** Resources (equal). **Huangjian Yi:** Data curation (equal). **Fengjun Zhao:** Formal analysis (equal). **Kang Li:** Resources (equal). **Lin Wang:** Resources (equal). **Xin Cao:** Supervision (equal).

DATA AVAILABILITY

Data underlying the results presented in this paper are not publicly available at this time but may be obtained from the corresponding authors upon reasonable request.

REFERENCES

- ¹P. Čerenkov, *Visible Luminescence of Pure Liquids under the Influence of γ -Radiation* (Dokl. Akad. Nauk SSSR, 1934), p. 451.
- ²J. S. Cho, R. Taschereau, S. Olma, K. Liu, Y.-C. Chen, C. K. Shen, R. M. Van Dam, and A. F. Chatzioannou, *Phys. Med. Biol.* **54**, 6757 (2009).

- ³S. B. Lee, S. B. Ahn, S.-W. Lee, S. Y. Jeong, Y. Ghilsuk, B.-C. Ahn, E.-M. Kim, H.-J. Jeong, J. Lee, and D.-K. Lim, *NPG Asia Mater.* **8**, e281 (2016).
- ⁴Z. Hu, M. Zhao, Y. Qu, X. Zhang, M. Zhang, M. Liu, H. Guo, Z. Zhang, J. Wang, and W. Yang, *J. Nucl. Med.* **58**, 169 (2017).
- ⁵J. S. Klein, G. S. Mitchell, and S. R. Cherry, *Phys. Med. Biol.* **62**, 4183 (2017).
- ⁶G. S. Mitchell, R. K. Gill, D. L. Boucher, C. Li, and S. R. Cherry, *Philos. Trans. R. Soc. London, A* **369**, 4605 (2011).
- ⁷A. Ruggiero, J. P. Holland, J. S. Lewis, and J. Grimm, *J. Nucl. Med.* **51**, 1123 (2010).
- ⁸S. Y. Jeong, M.-H. Hwang, J. E. Kim, S. Kang, J. C. Park, J. Yoo, J.-H. Ha, S.-W. Lee, B.-C. Ahn, and J. Lee, *Endocr. J.* **58**, 575 (2011).
- ⁹Y. Xu, E. Chang, H. Liu, H. Jiang, S. S. Gambhir, and Z. Cheng, *J. Nucl. Med.* **53**, 312 (2012).
- ¹⁰M. R. Grootendorst, M. Cariati, S. E. Pinder, A. Kothari, M. Douek, T. Kovacs, H. Hamed, A. Pawa, F. Nimmo, and J. Owen, *J. Nucl. Med.* **58**, 891 (2017).
- ¹¹S. R. Arridge, *Inverse Probl.* **15**, R41 (1999).
- ¹²C. Li, G. S. Mitchell, and S. R. Cherry, *Opt. Lett.* **35**, 1109 (2010).
- ¹³X. Ding, K. Wang, B. Jie, Y. Luo, Z. Hu, and J. Tian, *Biomed. Opt. Express* **5**, 2091 (2014).
- ¹⁴H. Zhenhua, M. Liu, H. Guo, Z. Zhang, and J. Tian, *J. Nucl. Med.* **57**, 59 (2016).
- ¹⁵J. Zhong, J. Tian, X. Yang, and C. Qin, *Ann. Biomed. Eng.* **39**, 1728 (2011).
- ¹⁶Y. Xu, H. Liu, and Z. Cheng, *J. Nucl. Med.* **52**, 2009 (2011).
- ¹⁷W. Cong, G. Wang, D. Kumar, Y. Liu, M. Jiang, L. V. Wang, E. A. Hoffman, G. McLennan, P. B. McCray, and J. Zabner, *Opt. Express* **13**, 6756 (2005).
- ¹⁸M. A. Naser and M. S. Patterson, *Biomed. Opt. Express* **2**, 3179 (2011).
- ¹⁹M. A. Naser and M. S. Patterson, *Biomed. Opt. Express* **1**, 512 (2010).
- ²⁰J. Liu, Y. Wang, X. Qu, X. Li, X. Ma, R. Han, Z. Hu, X. Chen, D. Sun, and R. Zhang, *Opt. Express* **18**, 13102 (2010).
- ²¹Z. Hu, J. Liang, W. Yang, W. Fan, C. Li, X. Ma, X. Chen, X. Ma, X. Li, and X. Qu, *Opt. Express* **18**, 24441 (2010).
- ²²H. Guo, X. He, M. Liu, Z. Zhang, Z. Hu, and J. Tian, *IEEE Trans. Med. Imaging* **36**, 1337 (2017).
- ²³H. Liu, X. Yang, T. Song, C. Bao, L. Shi, Z. Hu, K. Wang, and J. Tian, *J. Biomed. Opt.* **20**, 086007 (2015).
- ²⁴M. Cai, Z. Zhang, X. Shi, J. Yang, Z. Hu, and J. Tian, *IEEE Trans. Med. Imaging* **39**, 3207 (2020).
- ²⁵J. Shi, F. Liu, J. Zhang, J. Luo, and J. Bai, *J. Biomed. Opt.* **20**, 055004 (2015).
- ²⁶H. S. Mousavi, V. Monga, and T. D. Tran, *IEEE Signal Process. Lett.* **22**, 1903 (2015).
- ²⁷H. Guo, L. Gao, J. Yu, X. He, H. Wang, J. Zheng, and X. Yang, *J. Biophotonics* **13**, e201960218 (2020).
- ²⁸C. Huang, H. Meng, Y. Gao, S. Jiang, K. Wang, and J. Tian, "Fast and robust reconstruction method for fluorescence molecular tomography based on deep neural network," *Proc. SPIE* **10881**, 108811K (2019).
- ²⁹L. Guo, F. Liu, C. Cai, J. Liu, and G. Zhang, *Opt. Lett.* **44**, 1892 (2019).
- ³⁰Z. Zhang, M. Cai, Y. Gao, X. Shi, X. Zhang, Z. Hu, and J. Tian, *Phys. Med. Biol.* **64**, 245010 (2019).
- ³¹X. Cao, X. Wei, F. Yan, L. Wang, L. Su, Y. Hou, G. Geng, and X. He, *IEEE Access* **7**, 85178 (2019).
- ³²H. Meng, Y. Gao, X. Yang, K. Wang, and J. Tian, *IEEE Trans. Med. Imaging* **39**, 3019 (2020).
- ³³X. Zhang, M. Cai, L. Guo, Z. Zhang, B. Shen, X. Zhang, Z. Hu, and J. Tian, *Biomed. Opt. Express* **12**, 7703 (2021).
- ³⁴X. Zhang, C. Li, Z. Zhang, Z. Hu, and J. Tian, "Residual learning network for accurate and stable reconstruction in Cerenkov luminescence tomography," *Proc. SPIE* **12036**, 1203618 (2022).
- ³⁵S. Cai, Z. Mao, Z. Wang, M. Yin, and G. E. Karniadakis, *Acta Mech. Sin.* **37**, 1727 (2021).
- ³⁶A. D. Klose, *J. Quant. Spectrosc. Radiat. Transf.* **111**, 1852 (2010).
- ³⁷W. Cai, M. Xu, and R. R. Alfano, *IEEE J. Sel. Top. Quantum Electron.* **9**, 189 (2003).
- ³⁸Y. Lv, J. Tian, W. Cong, G. Wang, J. Luo, W. Yang, and H. Li, *Opt. Express* **14**, 8211 (2006).
- ³⁹W. Bangerth and A. Joshi, *Inverse Probl.* **24**, 034011 (2008).
- ⁴⁰D. Wang, X. Liu, Y. Chen, and J. Bai, *IEEE Trans. Inf. Technol. Biomed.* **13**, 766 (2009).
- ⁴¹A. X. Cong and G. Wang, *Opt. Express* **13**, 9847 (2005).
- ⁴²Y. Ma, D. Yu, T. Wu, and H. Wang, *Front. Data Comput.* **1**, 105 (2019).
- ⁴³X. He, J. Liang, X. Wang, J. Yu, X. Qu, X. Wang, Y. Hou, D. Chen, F. Liu, and J. Tian, *Opt. Express* **18**, 24825 (2010).
- ⁴⁴X. Cao, J. Zhang, J. Yang, C. Fan, F. Zhao, W. Zhou, L. Wang, G. Geng, M. Zhou, and X. Chen, *J. Appl. Phys.* **128**, 193104 (2020).
- ⁴⁵B. Parvitte, C. Risser, R. Vallon, and V. Zéninari, *Appl. Phys. B* **111**, 383 (2013).
- ⁴⁶S. Ren, X. Chen, H. Wang, X. Qu, G. Wang, J. Liang, and J. Tian, *PLoS One* **8**, e61304 (2013).
- ⁴⁷H. Yi, D. Chen, W. Li, S. Zhu, X. Wang, J. Liang, and J. Tian, *J. Biomed. Opt.* **18**, 056013 (2013).